JMEPEG (2026) 35:400–420
https://doi.org/10.1007/s11665-025-11599-3

1059-9495/$19.00

ORIGINAL RESEARCH ARTICLE

Influence of Vacuum Gas Nitriding on Wear and Corrosion Behavior of a High Manganese Steel

Cihangir Tevfik Sezgin and Fatih Hayat

Submitted: 11 January 2025 / Revised: 17 April 2025 / Accepted: 25 April 2025 / Published online: 1 July 2025

In this study, the wear and corrosion behavior of gas-nitrided high manganese steel (HMS) was investigated. Vacuum gas nitriding was carried out for surface treatment of HMS at 520 and 570 °C for 12, 18 and 24 h. The base metal contained α and ε martensite, while austenite was also observed in heat-treated base metal. Although all gas-nitrided samples contain Fe_3N, Fe_4N, γ, α and ε martensite, FeSi phase was only determined in N1-N6 samples. Expanded martensite and white layer (complex S phase) were observed in N1-N6 and N7-12, respectively. The gas-nitriding process significantly increased the surface hardness of HMS due to the iron nitride. Daimler-Benz Rockwell-C adhesion test shows that gas-nitriding HMS has sufficient adhesion behavior. The gas-nitriding process increases the wear and corrosion resistance of the HMS significantly.

Keywords corrosion, gas nitriding, high manganese steel, wear

1. Introduction

High manganese steel (HMS) was discovered by Sir Robert Hadfield in the late 19th century. From the past to the present, HMS has been widely used in mining and mineral excavation applications such as crusher jaws, hoppers, impact hammers and grinding mill liners (Ref 1, 2). Since HMS exhibits radically higher strength, toughness properties, wear and corrosion resistance in comparison to conventional carbon steels, it has been preferred in various industries such as automotive (Ref 3, 4), marine structure (Ref 5), slurry pipes (Ref 6) and LNG transporting (Ref 7) in recent years. Especially HMS offers a promising future for ballistic requirements and the protection of military vehicles because of its excellent energy absorption capacity and weight-reduction properties. Thyssen Krupp developed an innovative HMS armor plate which had high energy absorption ability. This ability provides additional protection against projectiles for civilian security, military and cash transport vehicles (Ref 8). Bestera and Stumpf reported that HMS armor plates had sufficient energy absorption against M193 projectiles at the appropriate thickness (Ref 9). Howell et al. (Ref 10) investigated the ballistic performance of a HMS perforated sheet with the ballistic quality of P900 armor steel to reduce vehicle weight. HMS provided the acceptance criteria for P900 steel and HMS can be potential candidates for MIL-A-46100 steels. Moreover, the superior energy absorption capacity of the HMS can provide innovation opportunities for use as blast protection for armored ground vehicles and anti-aircraft gun shields on warships. Despite its outstanding properties, the abrasive and corrosive media decrease the service life of HMS components. Since the replacement of HMS components during the service is a costly situation, the companies try to extend the service life of components. The surface treatments have been usually carried out to improve the wear and corrosion resistance of components and increase surface hardness which is significant for armor plates. Increasing the surface hardness improves the ballistic resistance of armor steel (Ref 11, 12).

The vacuum gas nitriding process is a traditional thermochemical surface treatment, and it has many advantages such as the simple, cost-effective process, high bond strength and absence of sample geometric requirements (Ref 13). Gas nitriding is carried out to increase the fatigue life, hardness, wear and corrosion resistance of metallic surfaces (Ref 14-16). The nitride-forming elements, such as chromium, aluminum, iron and titanium, interact with nitrogen and the nitride compounds occur as a result of these interactions on the surface of steel. Although the chemical composition of steel is significant for the effectiveness of nitriding, the gas nitriding process can increase the surface hardness about 250 $HV_{0.05}$ regardless of its chemical composition (Ref 15). Besides, the nitrite phases generally improve the corrosion, wear resistance and hardness of the steel, insignificant development or opposite effect has been observed in some studies. Alphonsa et al. reported that 2205 duplex stainless steel plasma nitrided above 400 °C lost its corrosion passivity (Ref 17). Riazi et al. (Ref 18) observed that the nitrided surface increased the solution pH with the formation of NH_4^+ that increased the corrosion rate of nitrided 17-4 PH steel. Yuan et al. (Ref 19) reported the gas nitriding process was applied to HMS, which contained approximately 3% Al and Cr each, the surface hardness increased only 67 HV in comparison to the core hardness.

The studies discussing the wear and corrosion behavior of gas-nitrided HMS are still very limited. Therefore, the present study is to shed more light on the effect of vacuum gas nitriding on the wear and corrosion behavior of HMS. Due to poor

Cihangir Tevfik Sezgin, Kastamonu Vocational School, Mechanical and Metal Technology, Kastamonu University, 37150 Kastamonu, Turkey; and **Fatih Hayat**, Faculty of Engineering, Mechanical Engineering, Karabük University, 78050 Karabük, Turkey. Contact e-mail: ctsezgin@kastamonu.edu.tr.

cooling conditions, carbides such as Mn_3C may form at grain boundaries, and these brittle formations negatively affect the performance of HMS for many applications. To prevent carbide formation, HMSs are heat treated at 1000-1100 °C (Ref 1, 2). Therefore, the effects of gas nitriding on HMS after heat treatment were also examined.

2. Experimental Methods and Materials

The production of HMS was mentioned in the previous articles (Ref 20, 21). HMS has the following chemical composition (wt.%): 0.278 C, 2.75 Si, 13.804 Mn, 0.017 S, 0.011P, 0.036 Ni, 0.195 Cr, 0.058 Mo, 0.092 Al, 0.067 Cu and balance Fe. The heat treatment process of cold-rolled HMS was carried out at 1000 °C for 30 min, followed by water quenching to avoid carbide precipitation (Ref 1, 2).

All samples were cleaned with acetone before nitriding. All the air in the furnace was evacuated with a pressure of 10 Pa. The vacuum gas nitriding was carried out at 520 and 570 °C for 12, 18, and 24 h using an atmosphere of 66.6% high purity (99.99%) ammonia (NH_3) and 33.4% N_2. Gas nitriding process was carried out in industrial vertical gas nitriding furnace. Ammonia flow rate was set as 6.0 m^3/h, furnace pressure was set as 24 mbar. Constant ammonia flow rate was preferred to see the effect of temperature and time on gas nitriding. Sample dimensions are 2.75x30x15 mm. Samples were mechanically polished with SiC sandpaper up to 1500 grade. HMSs were etched in 4% Nital solution for 30 and 5 s, respectively. The microstructural analysis of the sample was conducted with a scanning electron microscope (SEM-TESCAN MAIA3 XMU). The component of the nitride layer was studied by employing energy-dispersive x-ray spectrometry (EDX) microprobe within SEM. The phase constituents on the surface of nitrided samples were determined by x-ray diffraction (XRD-Rigaku Ultima IV diffractometer) using Cu Kα radiation. The thickness of nitrided layers was measured with SEM. The sample nomenclatures are exhibited in Table 1.

Vickers microhardness test was applied (Shimadzu HMV-G) for hardness measurement from surface to core. 50 g load was applied (HV 0.05) and each point was moved from the surface to the core with a distance of 10 mm. Then, hardness traces were measured automatically by the test device.

The adhesion of the nitrided layers was determined by the VDI 3198 indentation test applied to analyze the adhesion properties of nitride layers on HMS. The test was carried out to determine damage on the nitrided layer under a 150 kg load. Three indentations were carried out for each sample. After the adhesion test, the indentation craters of gas-nitrided HMS were observed by using SEM. The quality of indentation craters was

Table 1 List of gas-nitrided HMS samples (BM: base metal; ABM: annealed base metal)

Nitriding temperature, °C	Nitriding time, h	Heat treatment	Sample name
520	12		N1
520	18		N2
520	24		N3
570	12		N4
570	18		N5
570	24		N6
…	…		BM
520	12	✔	N7
520	18	✔	N8
520	24	✔	N9
570	12	✔	N10
570	18	✔	N11
570	24	✔	N12
…	…	✔	ABM

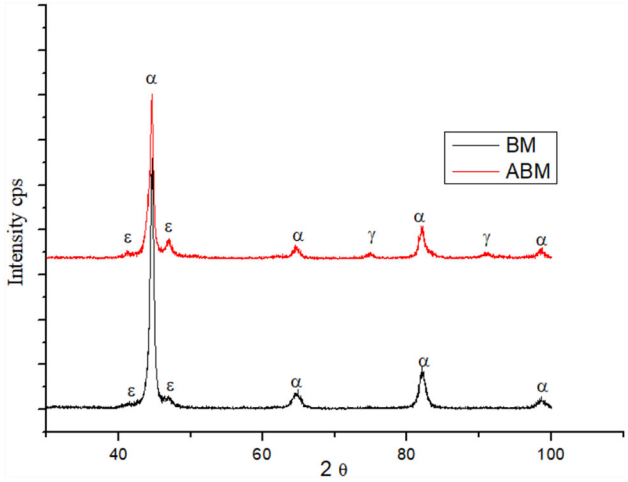

Fig. 1 XRD analyzes of BM and ABM

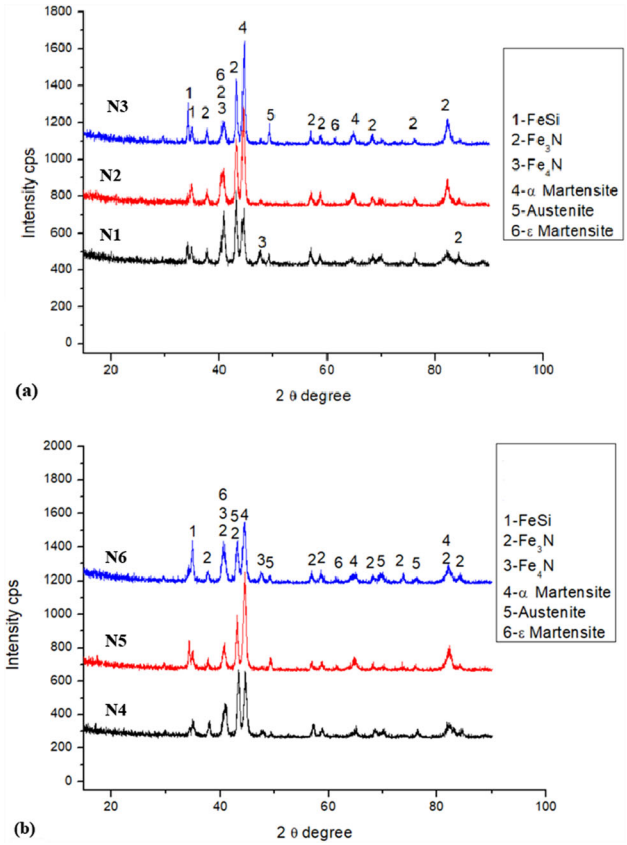

Fig. 2 XRD analyzes of cold-rolled and gas-nitrided HMS for (a) 520 °C, (b) 570 °C for the indicated durations

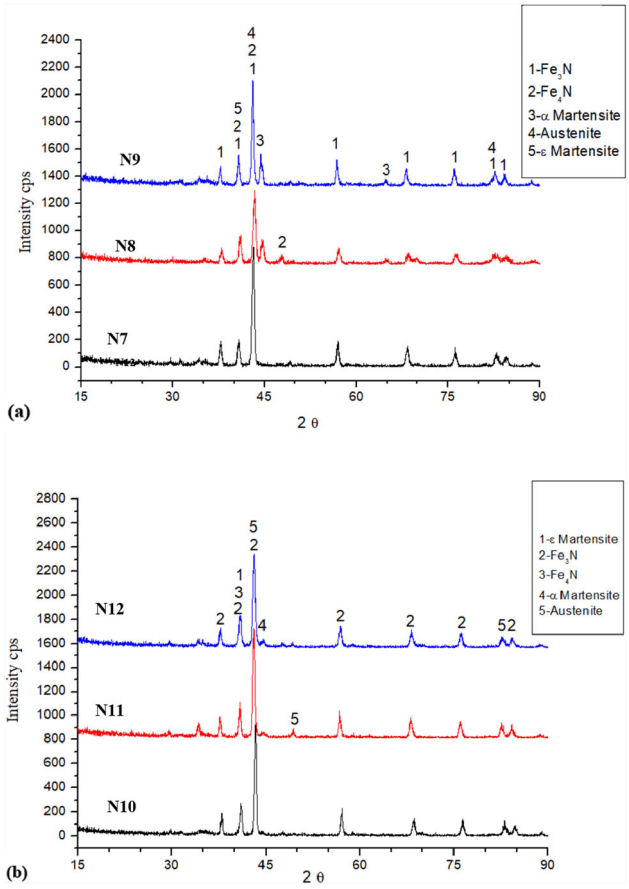

Fig. 3 XRD analyzes of heat treated and gas-nitrided HMS for (a) 520 °C, (b) 570 °C for the indicated durations

evaluated by the VDI 3198 quality map in Ref. (Ref 22). While the quality HF1-HF4 indicate strong interfacial adhesion, HF5 and HF6 indicate poor interfacial adhesion between the coating and the substrate (Ref 22).

The surface roughness was examined by a portable surface roughness tester (Mitutoyo SJ-410 series). At least three measurements were carried out to calculate the average roughness of the surfaces.

The wear behavior and coefficient of friction (COF) of all samples under dry sliding conditions were detected on a rectilinear reciprocating wear tester (Turkyus POD&HT&WT). Wear tests were carried out using 6 mm diameter WC abrasive balls on a rectilinear reciprocating wear tester. The wear tests were implemented under the load of 5, 10, and 15 N. Since the wear behavior of nitrided HMS was aimed to observe under different loads, the wear tests were applied under different loads. The total sliding distances on the specimens were 200 m for each loading. Each test was repeated three times. The wear volume loss and wear rate were determined by post-test analysis of the wear track measured using 3D profilometry. The wear rate was calculated according to:

$$R = V/ld \qquad \text{(Eq 1)}$$

R is the relative wear rate (mm^3/Nm), d is the sliding distance (m), V is the wear volume (mm^3) and l is the applied test load (N).

The corrosion behaviors of the surfaces were studied using polarization techniques (Tafel) with an electrochemistry station (Gamry Referans 3000 Potentiostat/Galvanostat/ZRA). Open-circuit potential (OCP) and Tafel for the substrate and the nitrided HMS were performed in 3.5 wt.% NaCl solution with three-electrode cells (working electrode: sample, reference electrode: Ag/AgCl and counter electrode: graphite). The

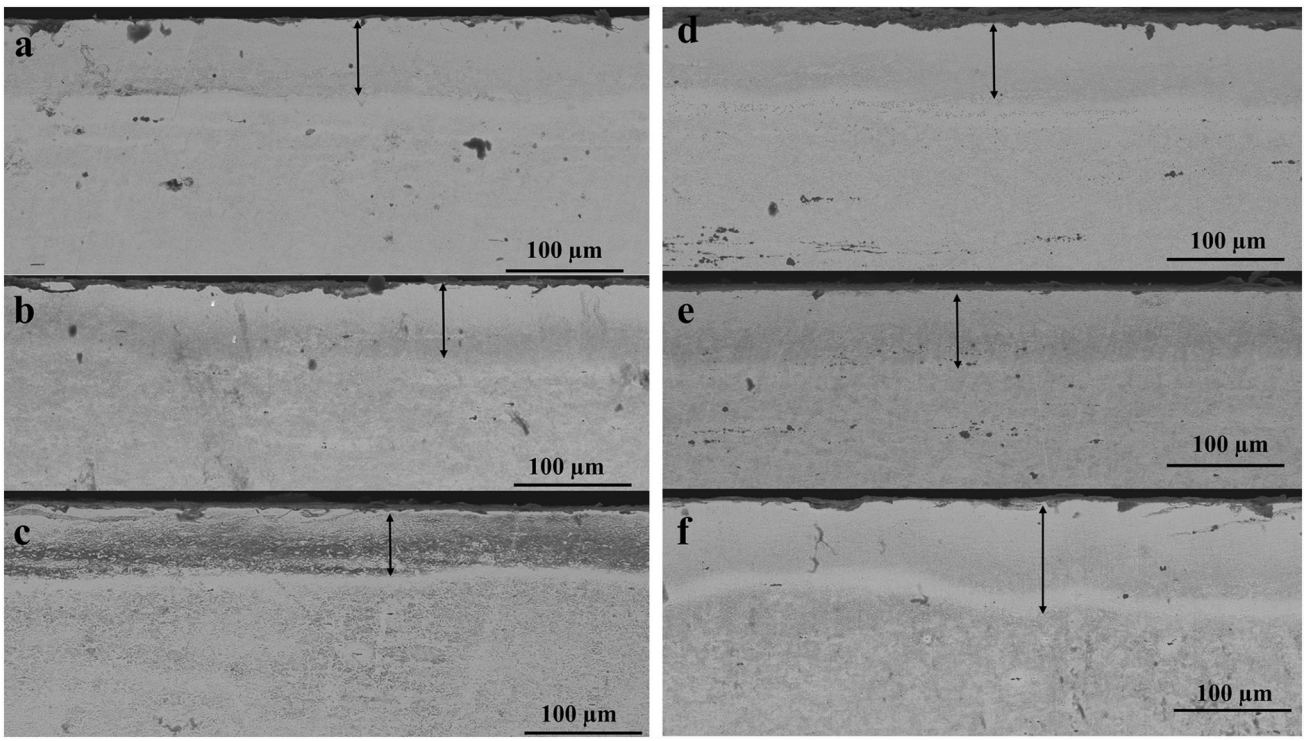

Fig. 4 SEM views of (a) N1, (b) N2, (c) N3, (d) N4, (e) N5, (f) N6

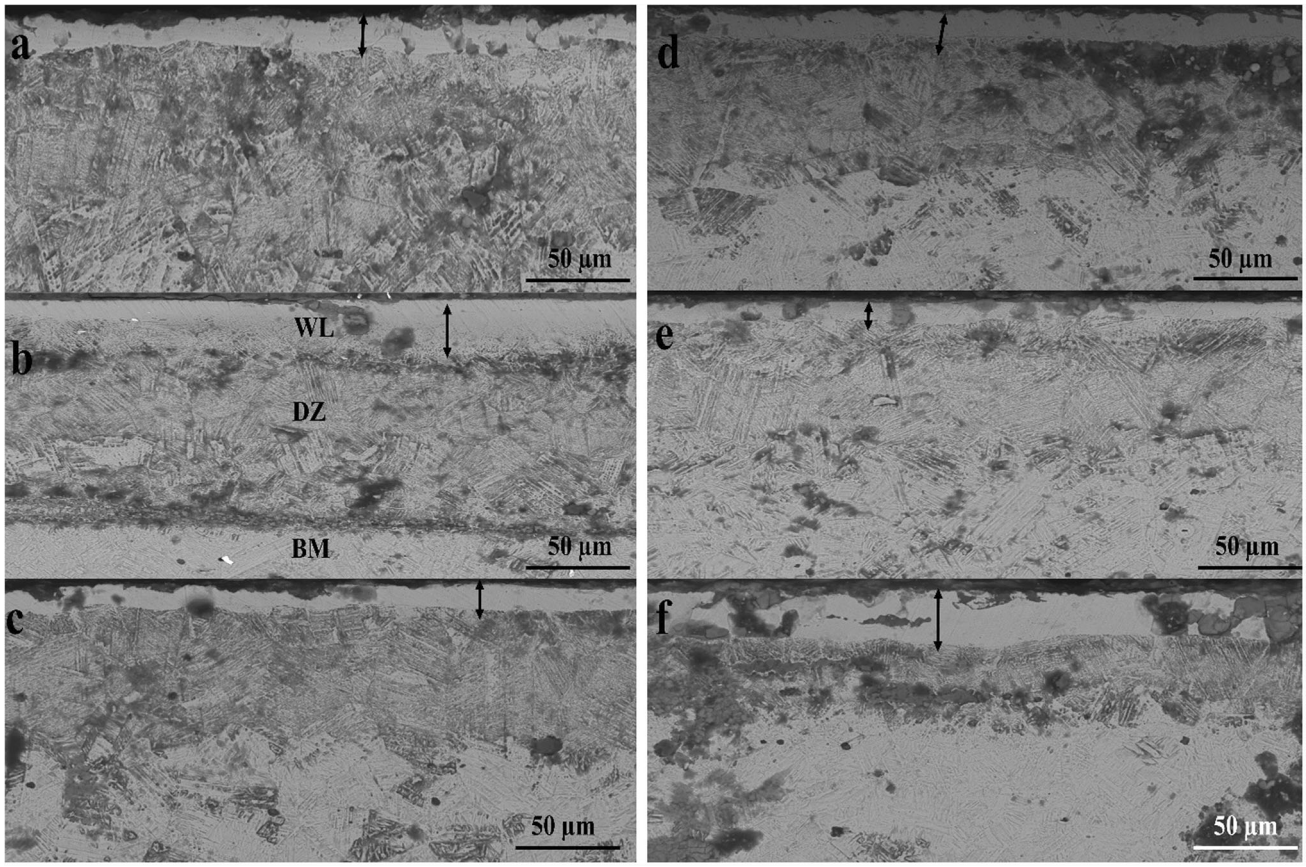

Fig. 5 SEM views of (a) N7, (b) N8, (c) N9, (d) N10, (e) N11, (f) N12 (WL: white layer; DZ: diffusion zone; BM: base metal)

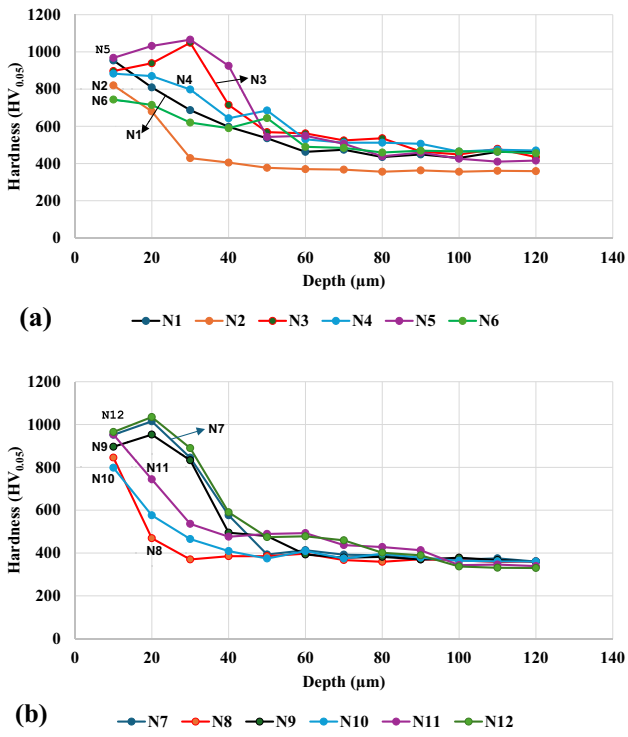

Fig. 6 Cross-sectional hardness measurements of (a) N1-N6, (b) N7-N12

surface area of the working electrode was 15 mm^2. The OCP measurements were made over a 3600-s period and plotted as a function of time after stabilization. The scanning rate in Tafel experiments was 1 mV/s relative to free corrosion potential from the cathodic potential of − 250 mV to anodic potential of + 250 mV.

Corrosion rates of samples are calculated using Eq 2:

$$\text{Corrosionrate} = \frac{3.27 \times \text{Icorr} \times \text{E.W.}}{A \times d \times 10^5} \quad \text{(Eq 2)}$$

*I*corr is the corrosion current density (A/mm^2), E.W. is the equivalent weight of the working electrode, d is the density of the working electrode (g/mm^3) and *A* is the working electrode area (mm^2)

3. Results and Discussion

3.1 Microstructural Characterization

Figure 1 indicates XRD analyzes of BM and ABM. While ε and α martensite phases were formed in BM, austenite phase was formed together with these two phases in ABM. In BM, high work hardening caused by cold rolling has resulted in the complete transformation of the austenite into new phases such as α and ε martensite. After heat treatment, austenite was observed in ABM. No carbide formation was observed in the XRD results.

Table 2 Gas-nitriding hardness depth values

Sample	White layer thickness (μm)	Method 1 nitriding hardness depth (μm)	Method 2 nitriding hardness depth(μm)
N1	*	50	70
N2	*	20	50
N3	*	80	90
N4	*	50	80
N5	*	70	90
N6	*	50	60
N7	12.54 ± 1.25	40	70
N8	23.76 ± 1.86	20	20
N9	12.16 ± 1.96	50	60
N10	12. 97 ± 1.04	30	80
N11	24.06 ± 1.95	70	90
N12	11.62 ± 1.53	70	90

*No white layer

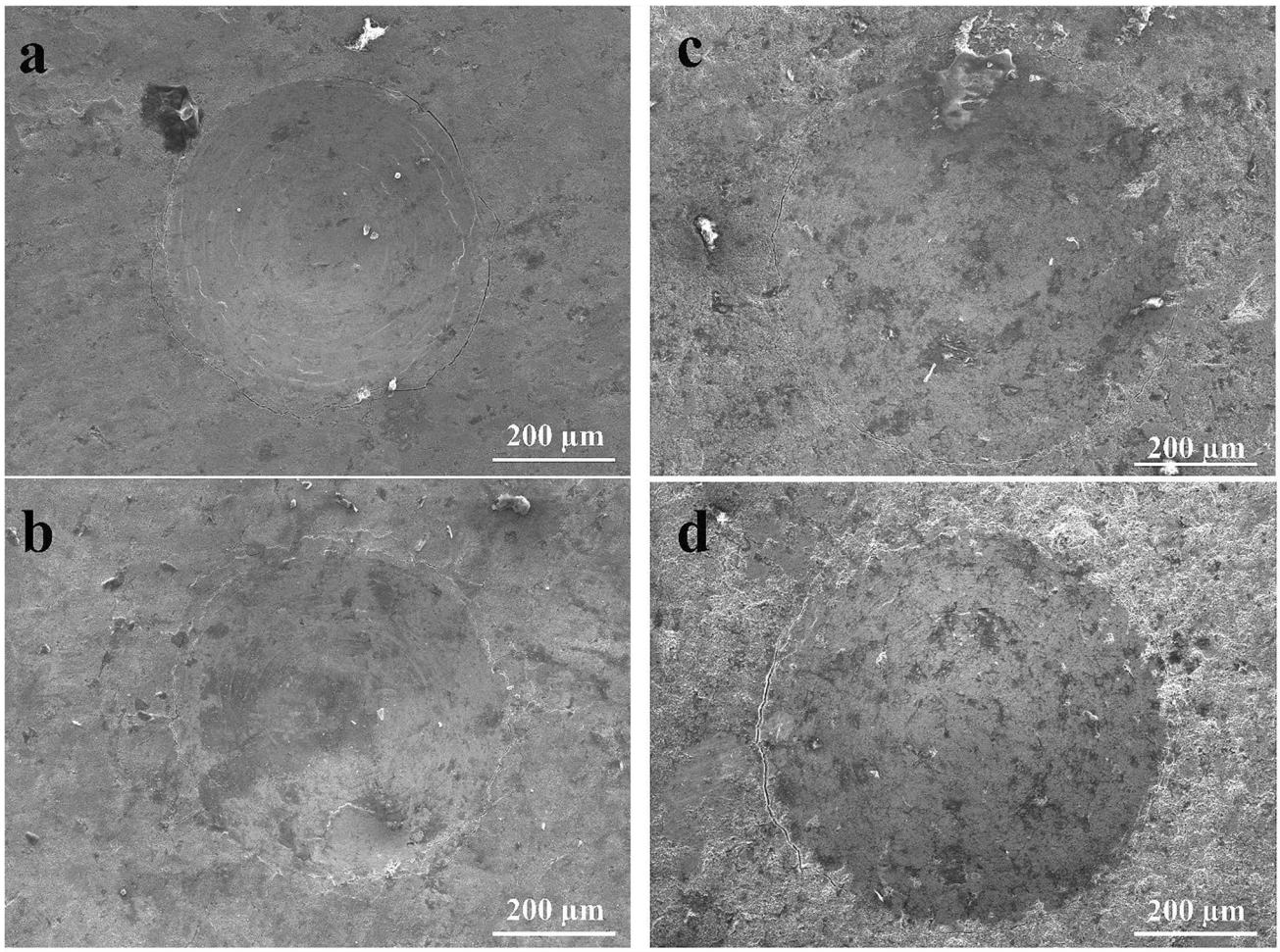

Fig. 7 SEM images of adhesion test of sample (a) N1, (b) N2, (c) N7 and (d) N8

Figure 2 and 3 shows the XRD analyses of N1-N6 and N7-N12 samples, respectively. FeSi, Fe_3N and Fe_4N are formed on the surface of gas-nitrided HMS. Only FeSi was not detected in N7-N9 samples. Unless the vacuum atmosphere existed, Fe_4N could not occur on the surface (Ref 23). Both the gas nitriding temperature above 400 °C (Ref 24) and the high ratio of Si in HMS resulted in the formation of FeSi, which is stable at room temperature (Ref 25). Also, alpha martensite (α) and austenite

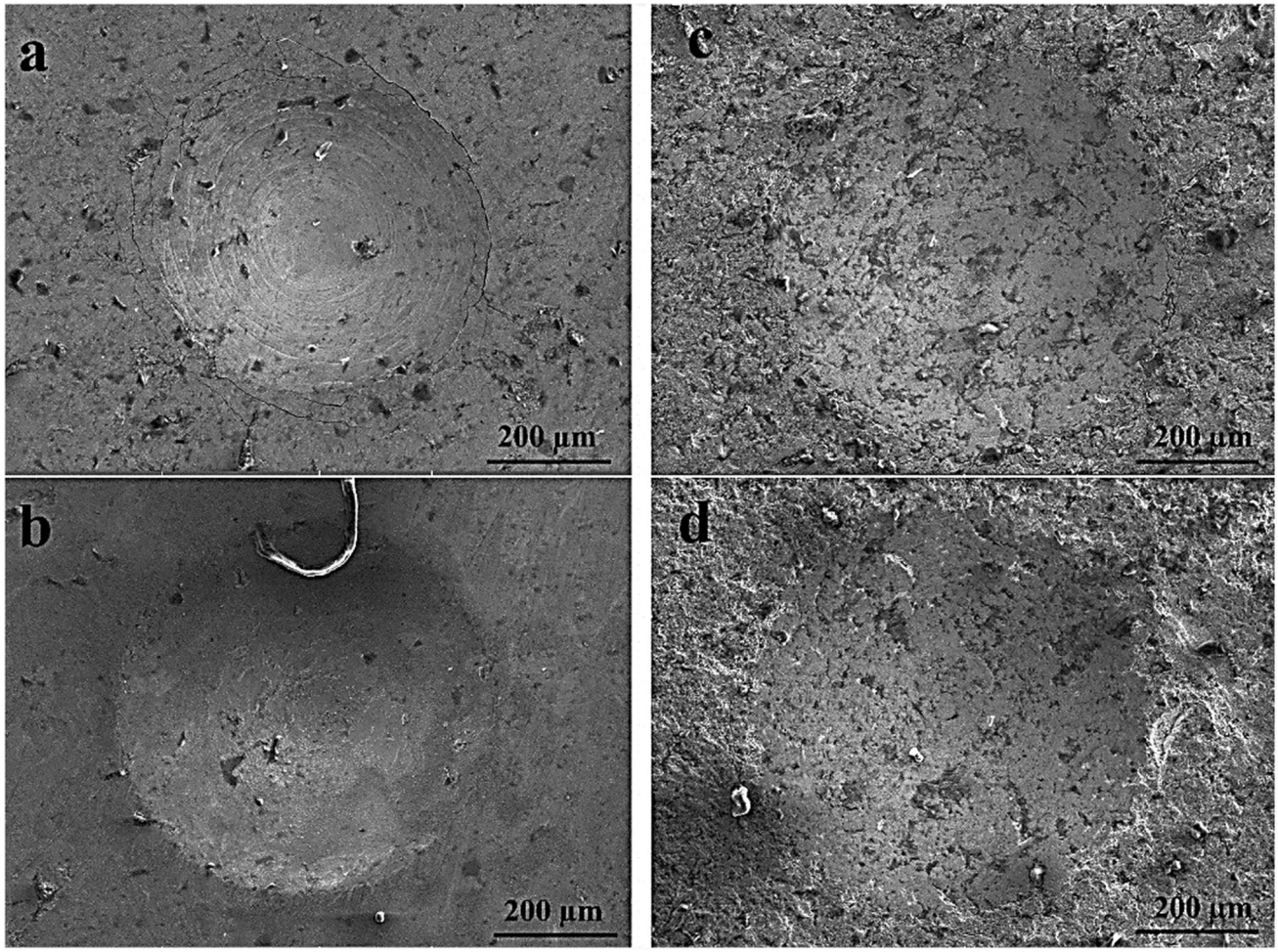

Fig. 8 SEM images of adhesion test of sample (a) N5, (b) N6, (c) N11 and (d) N12

Table 3 Average Ra and COF of samples (Ra; roughness)

Sample	Ra, μm	COF		
		5N	10N	15N
BM	0.356	0.506 ± 0.246	0.403 ± 0.246	0.359 ± 0.239
ABM	0.267	0.525 ± 0.252	0.507 ± 0.244	0.431 ± 0.236
N1	0.454	0.518 ± 0.229	0.481 ± 0.275	0.482 ± 0.297
N2	0.446	0.437 ± 0.242	0.480 ± 0.252	0.483 ± 0.264
N3	0.663	0.407 ± 0.231	0.321 ± 0.192	0.306 ± 0.187
N4	0.535	0.234 ± 0.177	0.193 ± 0.129	0.219 ± 0.138
N5	0.653	0.499 ± 0.273	0.487 ± 0.287	0.506 ± 0.281
N6	0.556	0.564 ± 0.280	0.569 ± 0.296	0.558 ± 0.286
N7	1.732	0.240 ± 0.164	0.344 ± 0.262	0.430 ± 0.278
N8	1.591	0.250 ± 0.202	0.475 ± 0.286	0.505 ± 0.265
N9	1.582	0.318 ± 0.270	0.412 ± 0.256	0.436 ± 0.264
N10	1.753	0.256 ± 0.182	0.300 ± 0.160	0.280 ± 0.201
N11	0.481	0.405 ± 0.226	0.442 ± 0.212	0.487 ± 0.270
N12	0.888	0.456 ± 0.267	0.524 ± 0.287	0.493 ± 0.262

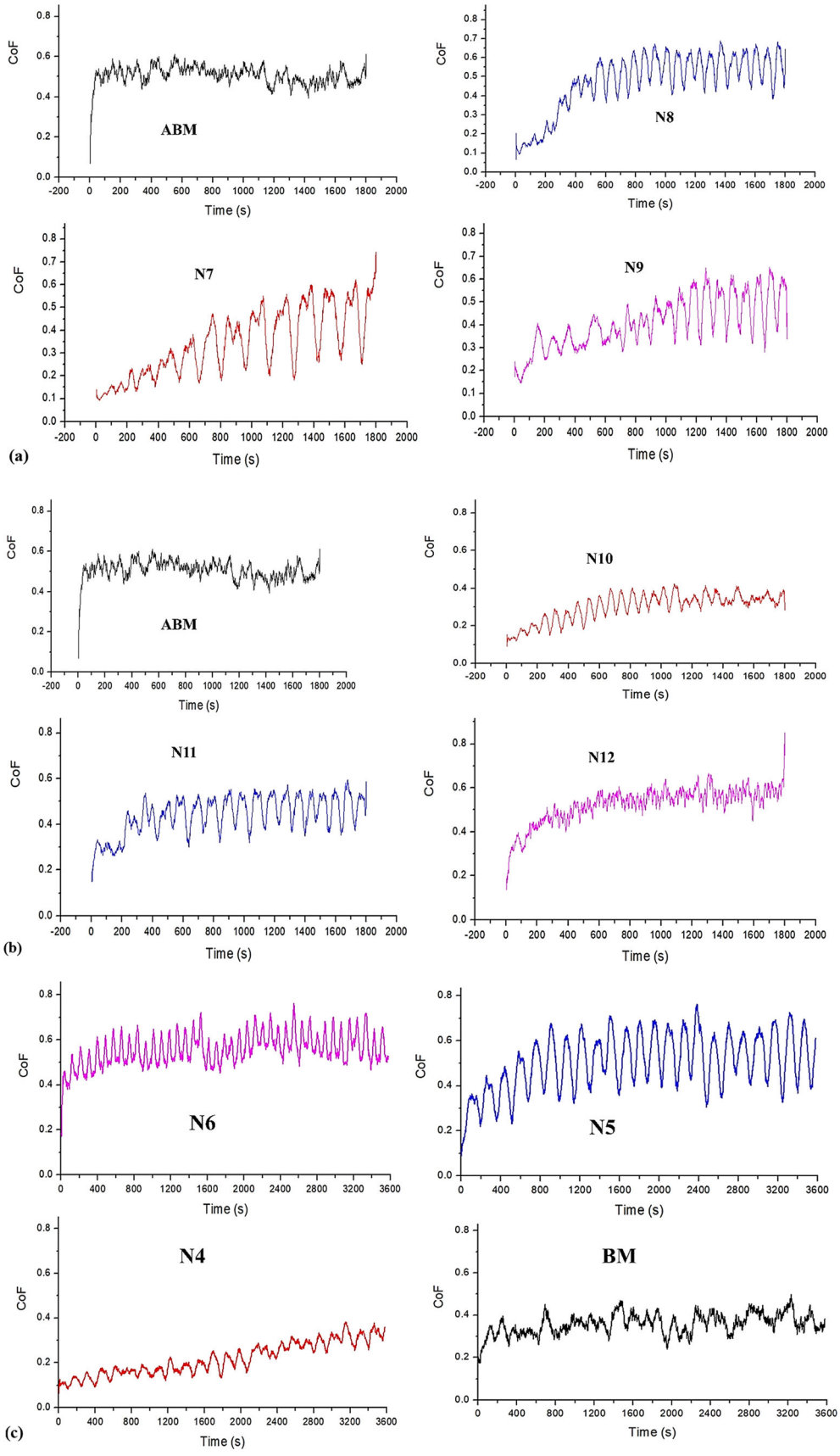

Fig. 9 COF curves of samples in wear test under (a) 5 N, (b)10 N, (c)15 N loads

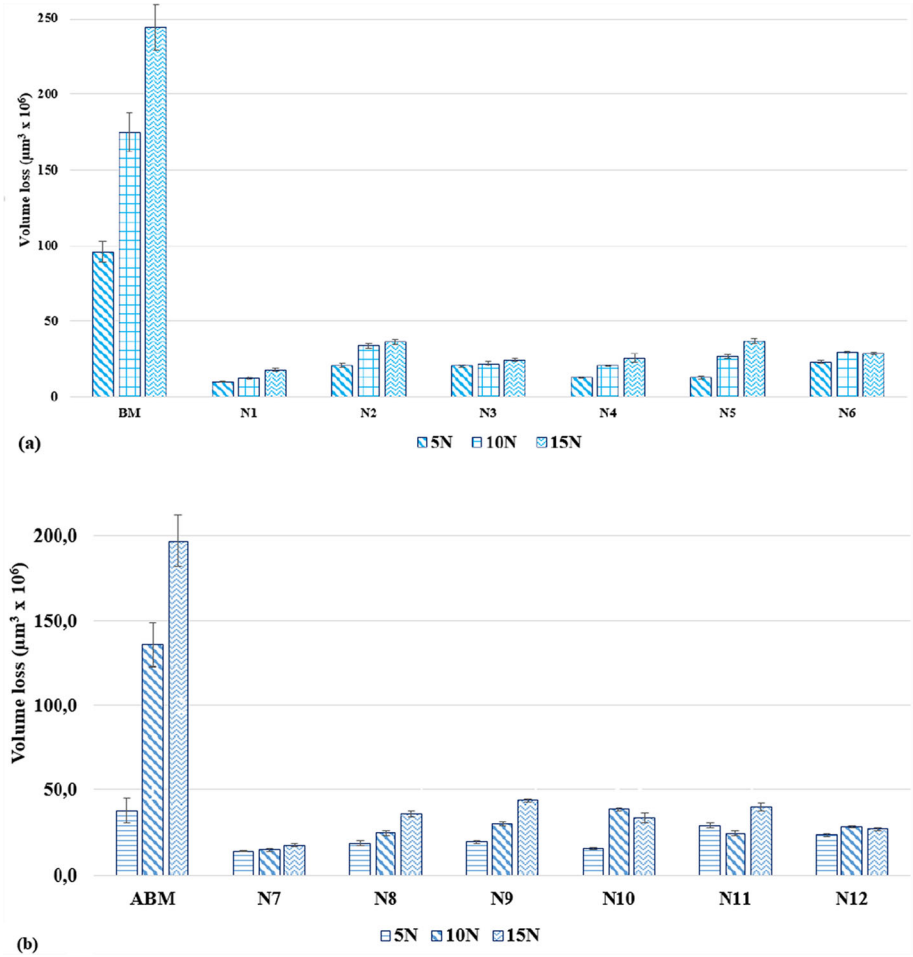

Fig. 10 Wear volume loss of (a) BM and N1-N6, (b) ABM and N7-12

(γ) were identified in XRD analyses of vacuum gas-nitrided HMS. While α and epsilon martensite (ε) were determined in the microstructure of HMS formed after cold rolling (Fig. 1), γ could not be identified by XRD. This XRD analysis uncovered the formation of γ in the structure of gas-nitrided HMS due to the high temperature and long processing time. Since nitrogen is an austenite stabilizing element (Ref 26), it may have contributed to the formation of austenite.

In Fig. 4, the white layer was not observed in the cross-sectional SEM microstructure of the cold-rolled, gas-nitrided HMS. In studies on nitriding of martensitic stainless steels in the literature, it has been observed that while a white layer is not formed, nitrogen-rich layer is formed (Ref 27-29). In this study, Fig. 1 shows that the microstructure is completely martensite in HMS after cold rolling, just like in martensitic stainless steel. Supersaturation of nitrogen promotes the expansion of face-centered cubic crystal lattice and the formation of residual stresses or expanded martensite in austenitic and martensitic stainless steels. This layer is called "expanded martensite" (Ref 29).

Figure 5 shows the cross-sectional SEM view of heat treated and gas-nitrided HMSs. Unlike the cold-rolled HMSs, it was observed that the heat treated HMS had a white layer on the surface after the gas nitriding process. In addition, a diffusion zone was formed under the white layer. The formation of the white layer after gas nitration in heat treated HMSs was

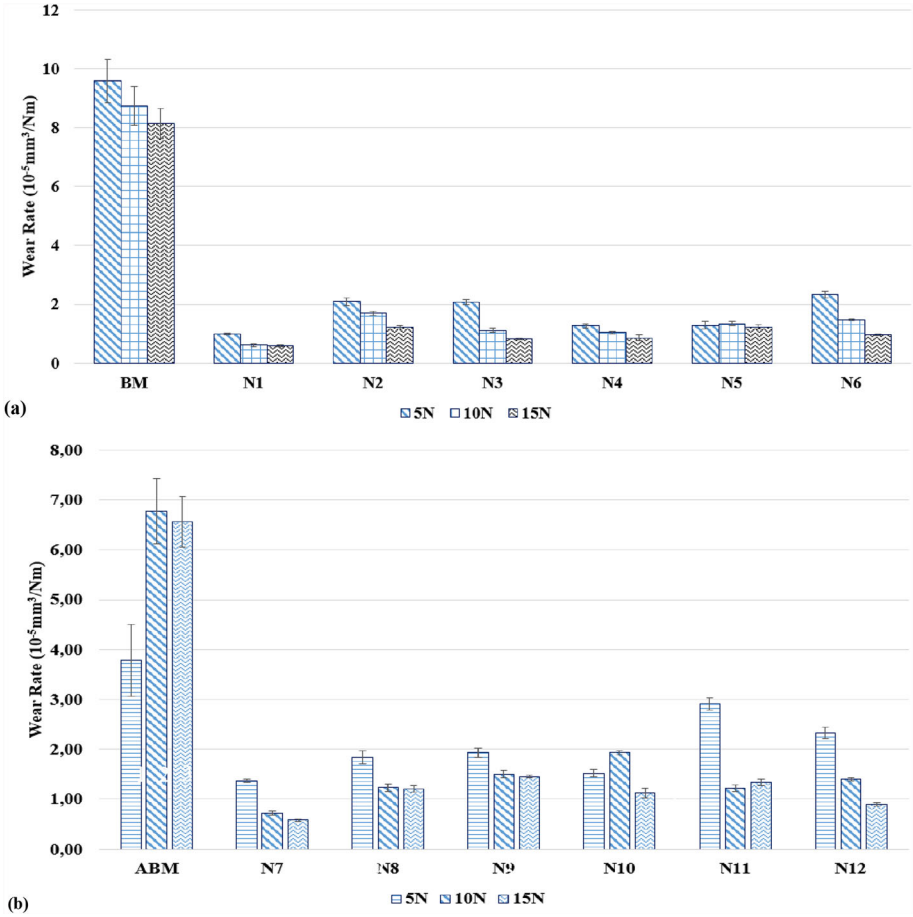

Fig. 11 Wear rates of (a) BM and N1-N6, (b) ABM and N7-12

attributed to the presence of austenite in the microstructure. It is known that nitrogen-rich phase white layer called "S phase" or "expanded austenite" is formed after gas nitriding in austenitic stainless steel (Ref 30-32) and TWIP steel (Ref 33), which is an austenitic HMS. As the nitriding temperature increases, especially above 400 °C, the XRD peaks shift to a lower angle since interstitial nitrogen atoms cause the lattice distortion of the austenite (Ref 33). However, this white layer does not consist of pure S phase. It is a complex phase that also contains Fe_3N, Fe_4N and ε martensite.

The cross-sectional microhardness profiles are shown in Fig. 6. The hardness of BM and ABM were 532 and 356 $HV_{0.05}$, respectively. The highest hardness value was observed at N12 and N5 (1035 and 1032 $HV_{0.05}$, respectively). Although the minimum surface hardness was observed in the N6 sample, its hardness is 1.5 times higher than BM. The gas-nitriding increased the surface hardness significantly due to the iron nitride forming. Although increasing gas nitriding temperature improves the diffusivity of nitrogen in the sample and causes the forming of iron nitrides along a diffusion zone with greater depth (Ref 34), in this study, no correlation was observed for the effect of increasing neither temperature nor time on surface hardness.

The determination of nitriding hardness depth has been presented in the literature with 2 methods. The first one of the methods accepts the boundary of the nitrided layer where the

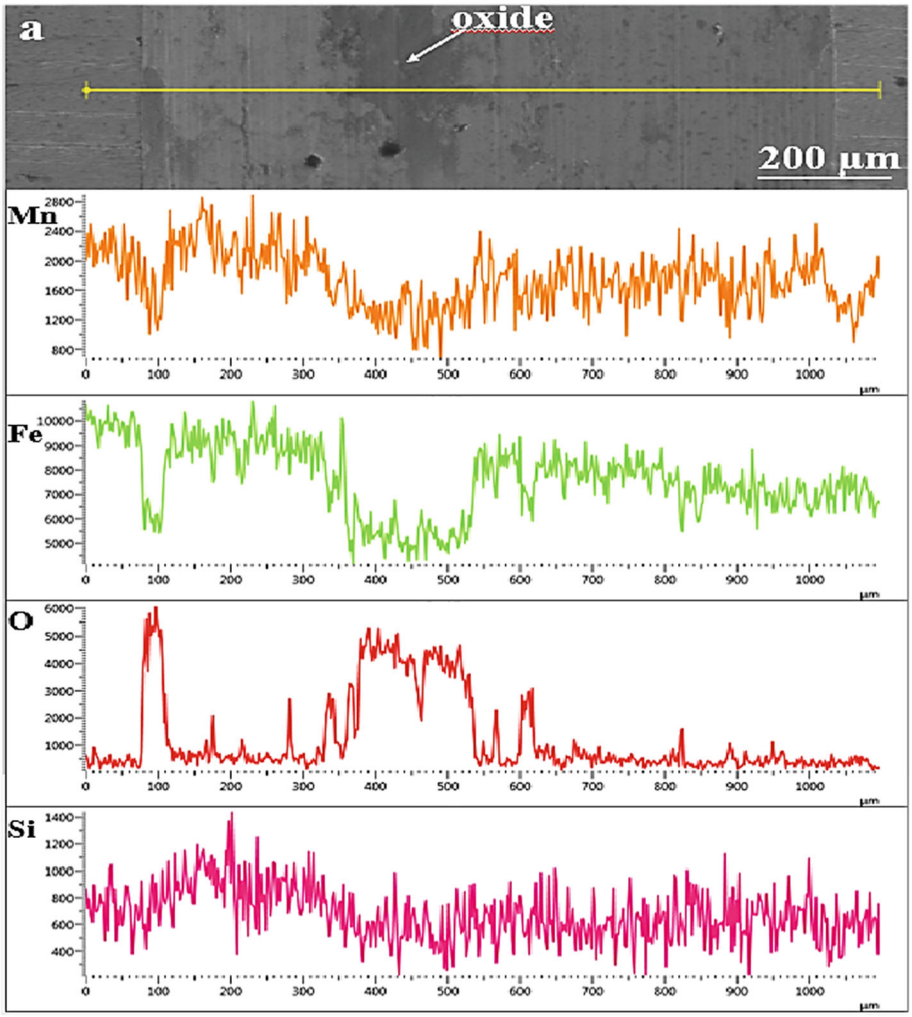

Fig. 12 Wear track EDX line analyzes of (a) BM with 10 N, (b) ABM with 15N load applied (horizontal axis label is μm)

hardness limit of 50 HV is above the core hardness. According to Method II, the limit of the nitrided layer should be 10% higher hardness than the core hardness (Ref 35, 36). The nitriding hardness depth and white layer thickness are shown in Table 2.

3.2 Adhesion Properties

Figure 7 and 8 shows the SEM images of the indentation track after the VDI 3198 Rockwell-C adhesion test. In Fig. 7 and 8a, b, c and d, many samples had no radial cracks, while others had very few (Fig. 7a, d and 8a). All samples exhibited almost perfect adhesion behavior. Neither flaking nor delamination occurred in the indentation crater because of strong interfacial bonds between the nitrided surface and HMS. Moreover, both increased gas nitriding time and temperature did not affect the adhesion behavior of samples. A successful coating depends on sufficient adhesion behavior between the substrate and the coating. Applied load and the contact geometry cause shear stresses at the interface. Although suitable coatings success to resist the shear stresses and forestall delaminations, weak interfacial adhesion causes delaminations at the indentation tracks (Ref 22). According to the VDI 3198 indentation test, the adhesion strength of all gas-nitrided sample surfaces corresponded to HF1 quality.

3.3 Friction Coefficient and Roughness

Table 3 exhibits both the roughness and COF of the samples. It was determined that the roughness values of BM and ABM

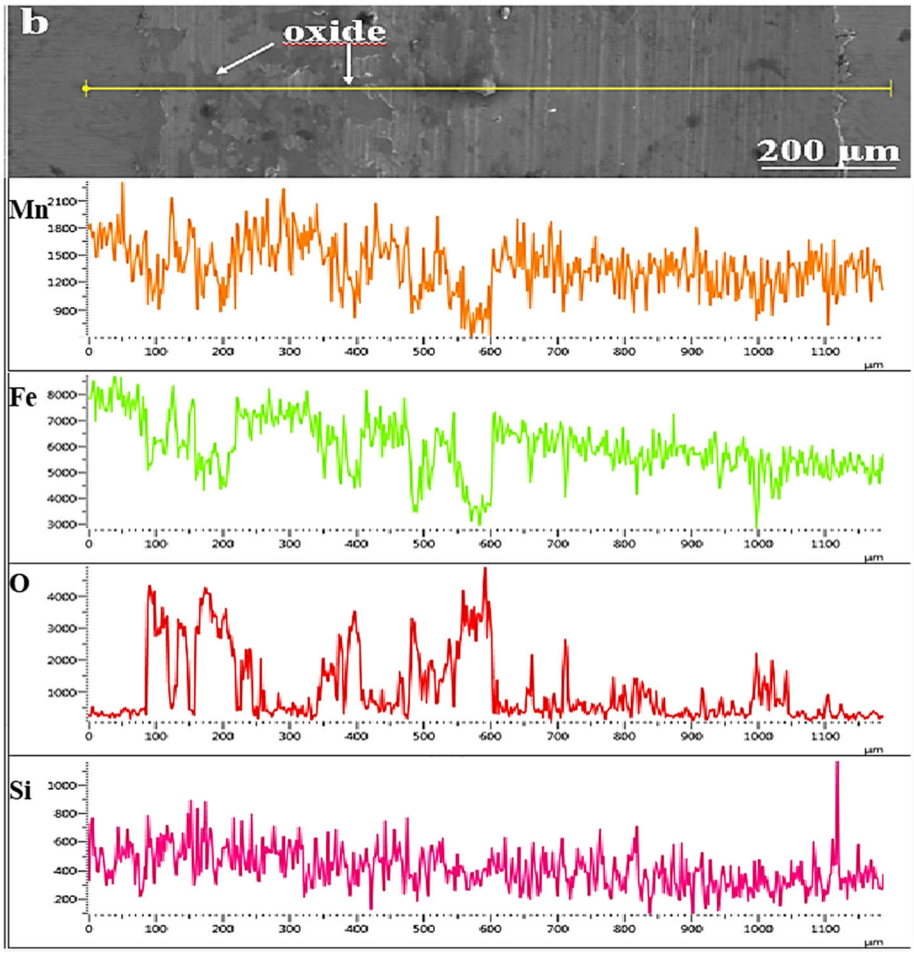

Fig. 12 continued

were lower than all gas-nitrided samples. The roughness of N1-N6 samples was lower than that of N7-12. Figure 9 shows the coefficient of friction (COF) graphs recorded during wear tests of all samples, which were tested under 5 N, 10, and 15 N loads. It was observed that the samples with the highest roughness (N7, N8, N9 and N10) had the lowest COF. Figure 9 shows that the variation of COF exhibits unstable states in all samples. Parameters such as high hardness, the adhesion strength of the coating, and surface roughness affect the COF (Ref 37). It was attributed that the high roughness prevented direct contact between the surfaces of the sample and the WC abrasive ball. Moreover, there are many zigzags in Fig. 9. When the abrasive ball contacts the sample, plastic deformation occurs and causes a shear force resulting in peaks in the graphs. Thanks to the shear force, the layer breaks and a downward peak is formed. In Fig. 9(a), (b), and (c), the samples whose names are written in the upper left corner of the COF graphs are shown as 1, 2, 3, 4, respectively, from top to bottom in each graph.

3.4 Wear Behavior

The volumetric wear loss results from reciprocating wear tests are shown in Fig. 10. In Fig.10, columns 1, 2, and 3 represent the wear test results caused by a load of 5, 10, and

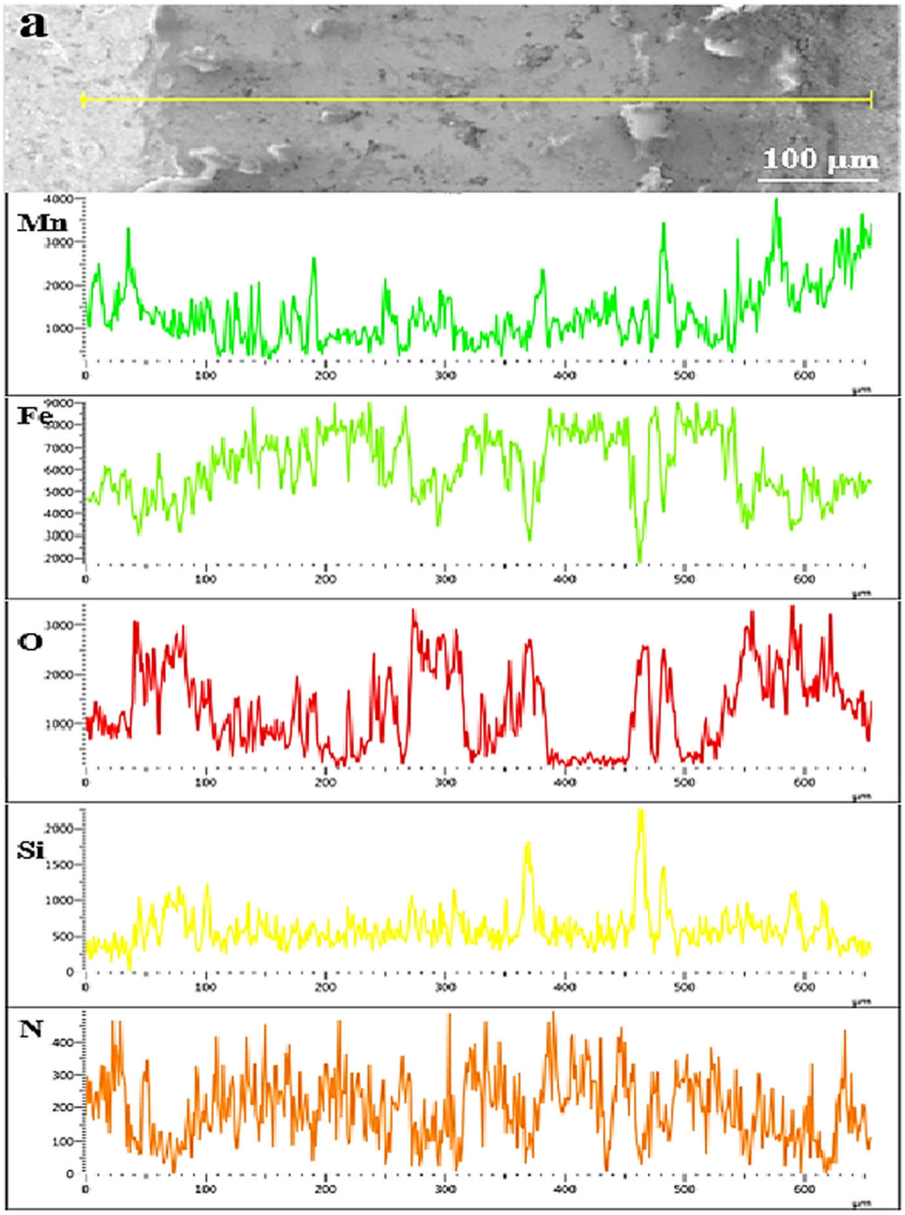

Fig. 13 Wear track EDX line analyzes of (a) N1, (b) N5 with 15N load applied (horizontal axis label is μm)

15 N, respectively. It indicates that an increase in the applied load increases the volumetric wear losses of all samples.

As seen in Fig. 1, while ABM contains γ, ε and α martensite, BM consists of ε and α martensite. The plastic deformation can transform from γ to ε or α martensite in the HMS. These transformations may have occurred instead of less wear loss in ABM according to BM because of the applied load (Ref 38).

It was observed that all gas-nitrided HMSs had lower wear volumes than BM and ABM at wear tests under 5, 10 and 15 N loads. The wear volume of gas-nitrided samples is drastically minimized due to the increase in surface hardness caused by forming white layer and expanded martensite. While the lowest volumetric wear loss was observed in N1 under each load, the highest volumetric wear loss was determined in BM. Among

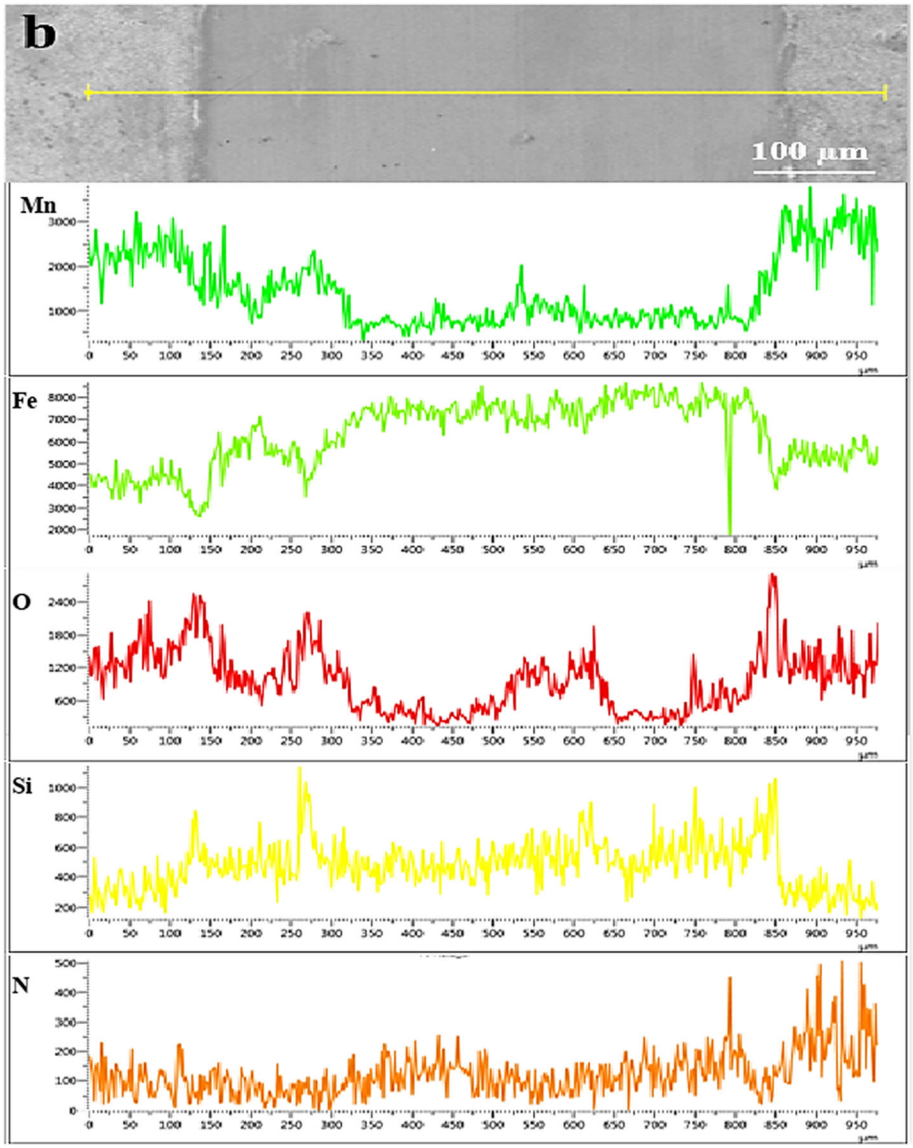

Fig. 13 continued

the gas-nitrided samples, the highest wear volumes were observed in N11, N10 and N9 samples under 5, 10 and 15 N loads, respectively.

No correlation was observed between the increase or decrease in wear resistance with changing gas nitriding temperature and time. In the gas nitration process, the diffusion of nitrogen increases with increasing temperature and time. Therefore, the deeper penetration of nitrogen atoms causes intense reaction media with the strong nitride-forming elements and they affect the wear performance of the substrate surface.

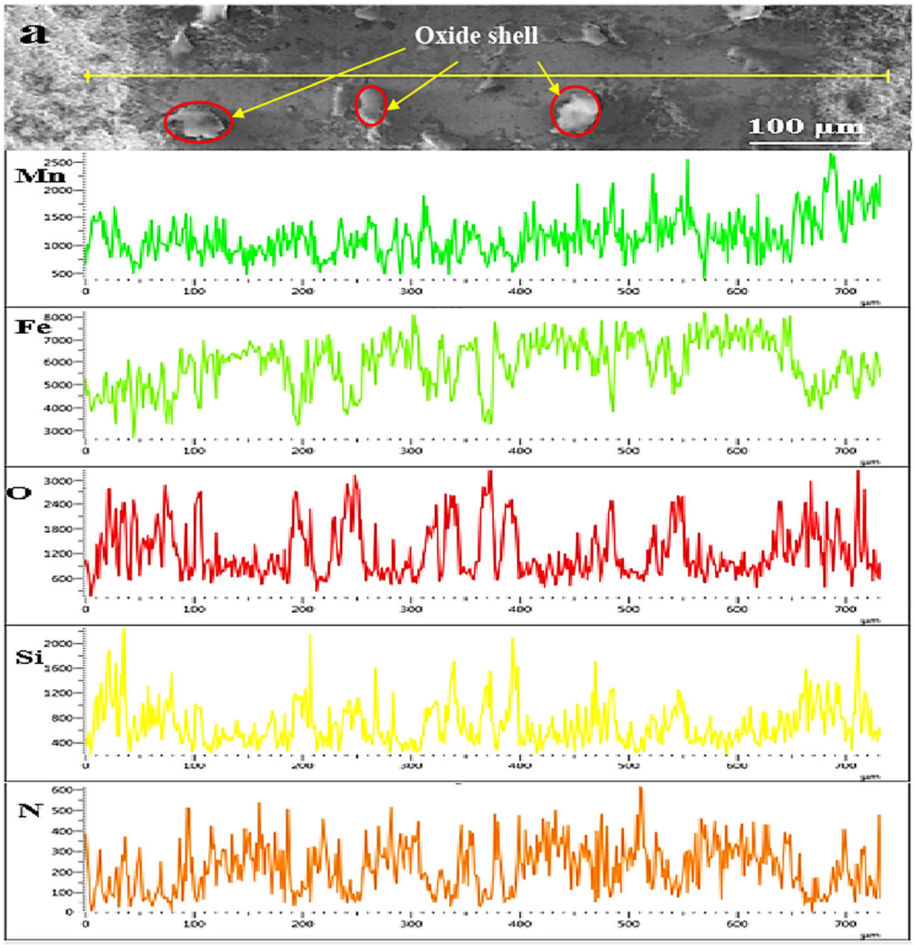

Fig. 14 Wear track EDX line analyzes of (a) N9 with 10 N, (b) N10 with 5N load applied (horizontal axis label is μm)

The fact that there is no correlation in wear performance despite increasing gas nitriding temperatures and times can be attributed to the absence of alloying elements (such as aluminum, vanadium, titanium, and chromium) in HMS that will form strong nitrides.

The wear rate values of gas-nitrided samples are shown in Fig. 11. In Fig. 11, columns 1, 2, and 3 represent the wear test results caused by a load of 5, 10, and 15 N, respectively. While N1 had the minimum wear rate, the highest wear rate was determined in BM for each load. Since the expanded martensite surface (N1-N6) and white layer (N7-12) increase the hardness of the surface, the wear resistance of HMS improves. Wear test results under 15 N load indicate that the gas-nitriding process improves the wear resistance of cold-rolled and heat-treated HMS. Among the gas-nitrided samples, even the N9 sample, which had the highest wear rate under 15 N load, was observed to have 5 and 4 times wear resistance compared to BM and ABM, respectively.

After the reciprocating wear test, EDX line and mapping analyses were performed on the wear tracks to determine the changes in the amount of existing elements on the surface of the samples. Figure 12(a) and (b) shows the EDX line analysis with a 10 and 15 N load applied to BM and ABM, respectively. When the SEM wear track of the samples was examined, the

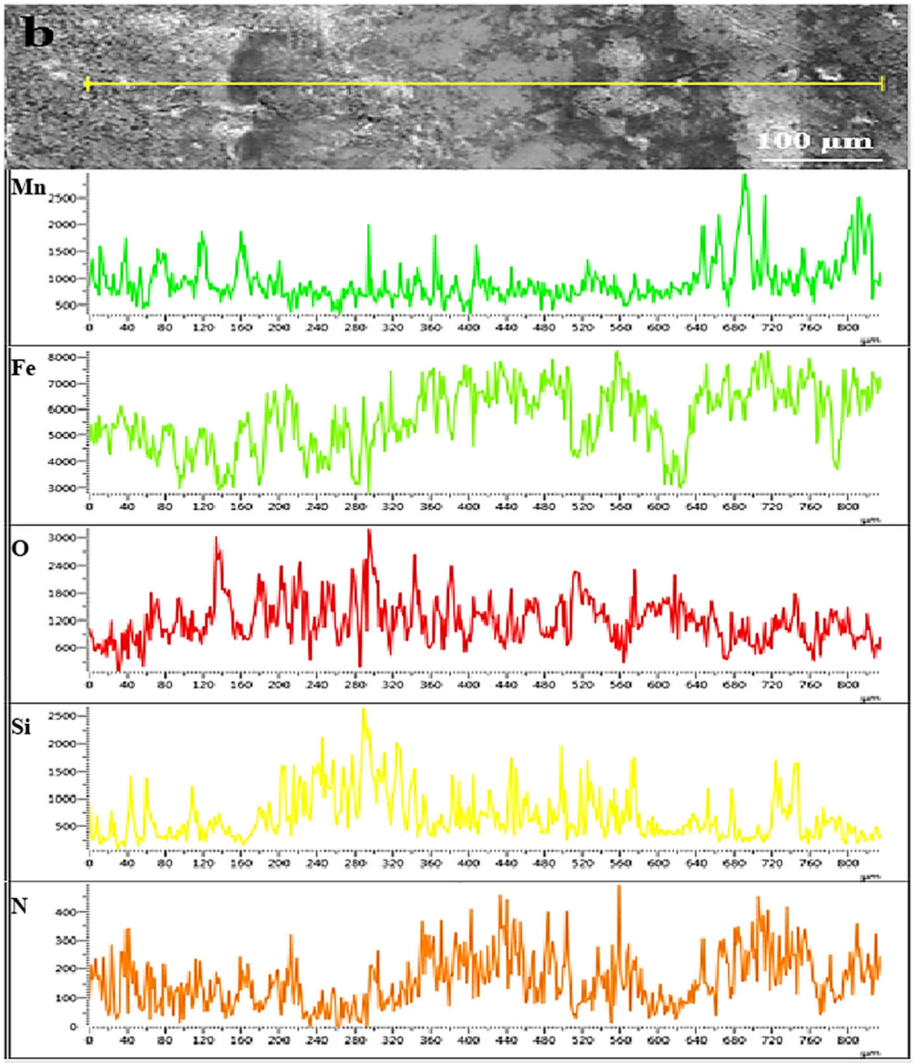

Fig. 14 continued

wear track of ABM (1055 μm) was wider than that of BM (1081 μm) due to the application of more load. The fluctuation in the amount of manganese and iron is similar to each other. The oxides are seen as dark layers in both samples.

Figure 13(a) and (b) indicates EDX line analyses obtained from the wear track formed as a result of the wear test applied to N1 and N5 under 15 N load, respectively. According to the EDX line analysis, the nitrogen content of N1 is higher than N5, both in the wear track and on the unworn surface. Manganese content decreased considerably along the wear trace in both samples. It was determined that oxygen increased significantly in the zones where iron considerably decreased. Iron oxide layers probably formed on the worn surface during the reciprocating wear test.

Figure 14(a) and (b) indicates EDX line analyzes obtained from the wear track formed as a result of the wear test applied to N9 and N10 under 10 and 15 N load, respectively. Manganese content decreased considerably along the wear trace in both samples such as N1 and N5. While oxide shell layers were formed in N9, they were not detected in N10. The fluctuation of nitrogen and silicon amounts did not show any significant change along the wear track.

Figure 15 exhibits the wear traces SEM views of BM (Fig. 15a, b and c) and ABM (Fig. 15d, e and f). In the wear test applied under 5N load, microcracks and delamination were observed in BM (Fig 15a), while debris and microcracks occurred in ABM (Fig 15d). In the wear test with 10 N load, delaminations increase in BM (Fig. 15b), while the surface is completely composed of grooves under 15 N load (Fig. 15c). The abrasive oxidative type wear mechanism occurred in BM. Oxidative wear caused by oxygen in the atmosphere is a common wear mechanism on metals. Microcracks were formed at the edge of the oxide layers. As the reciprocating wear test continued, microcracks caused delaminations and increase applied test load caused increased delaminations due to the oxide layers being removed from the surface.

In the applied wear test under 10 N load, delamination and grooves were formed in the ABM where the oxide layers were broken. However, in the test under 15 N load, it is seen that the surface is not replaced completely grooves as in BM, and the delamination of the oxide layers continues. Groove occurs with penetration of hard asperities of a harder counter body into the softer surface of a solid in sliding contact (Ref 23). Grooves show that abrasive wear occurs on the surface of BM and ABM.

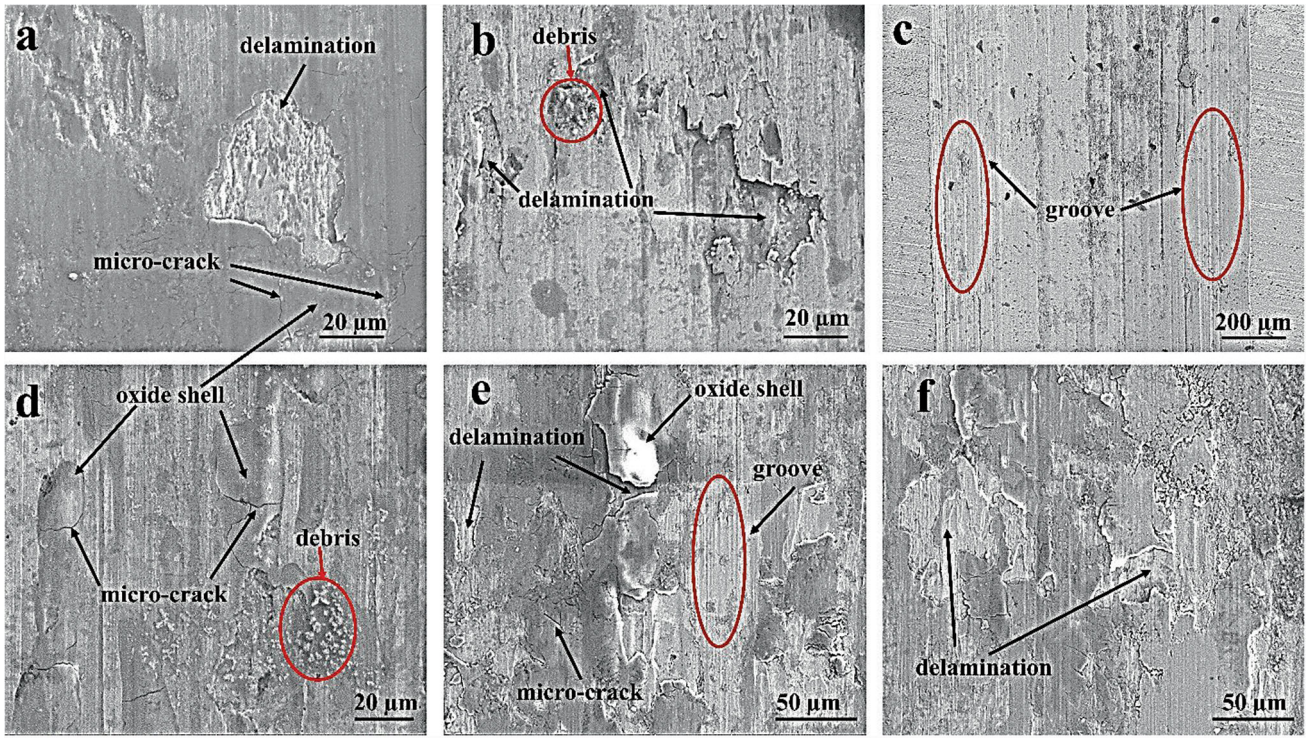

Fig. 15 SEM micrographs of the worn surfaces of (a, d) BM, ABM under 5 N, (b, e) BM, ABM under 10 N and (c, f) BM, ABM under 15 N load

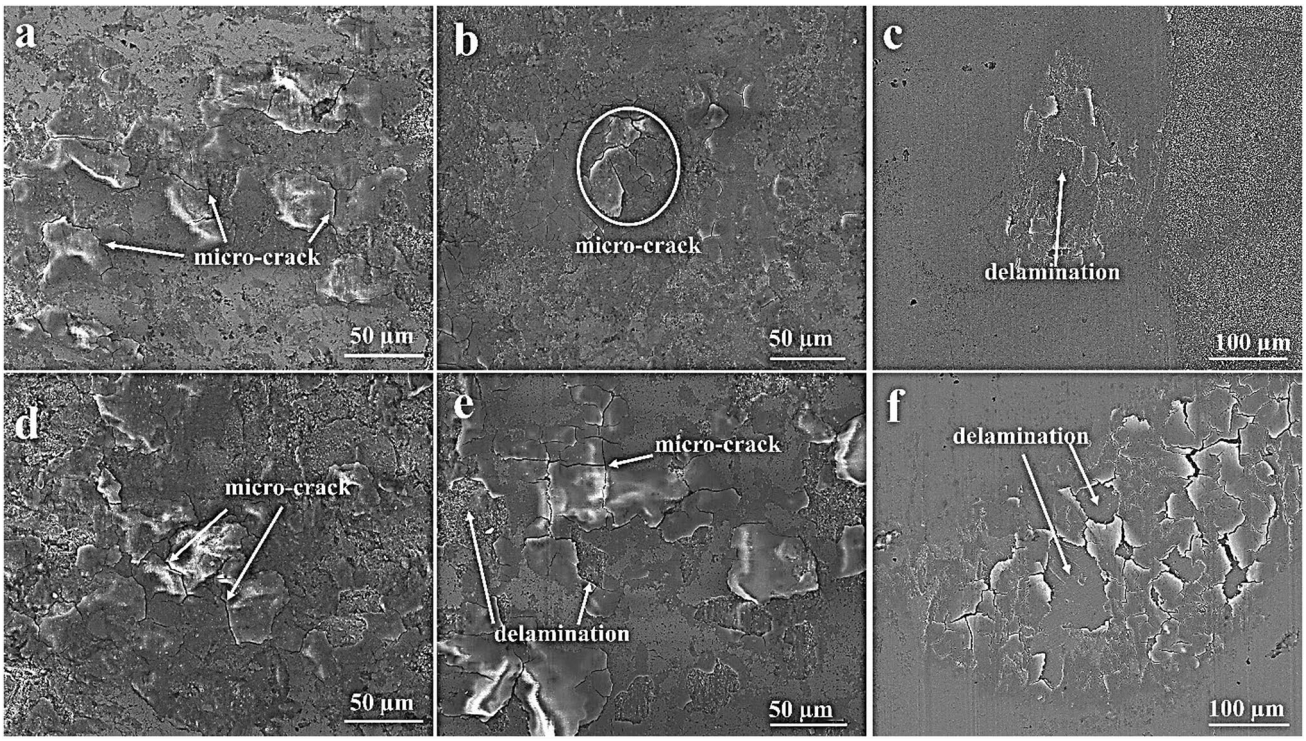

Fig. 16 SEM micrographs of the worn surfaces of (a, d) N1, N8 under 5 N, (b, e) N4, N9 under 10 N and (c, f) N6, N11 under 15 N load

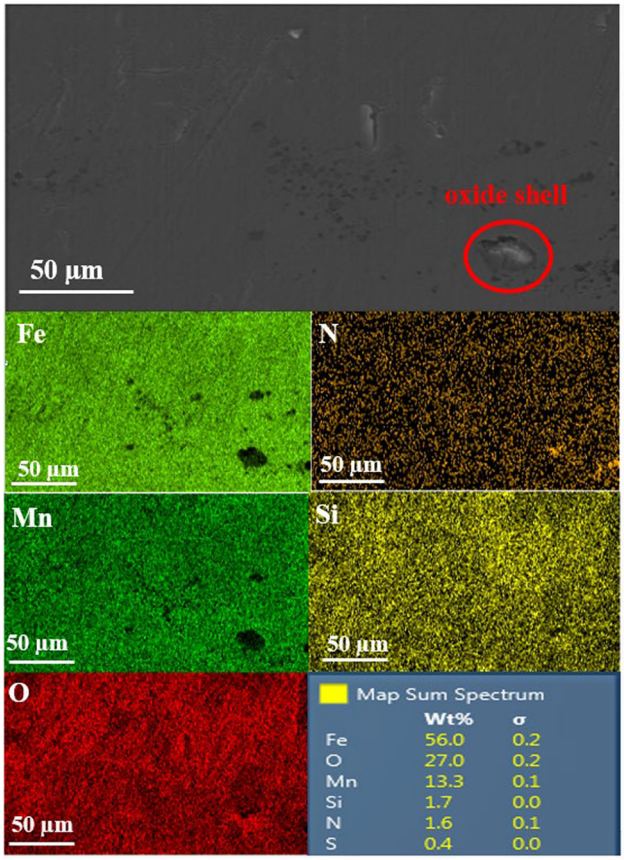

Fig. 17 EDX local mapping of N12 after the wear test

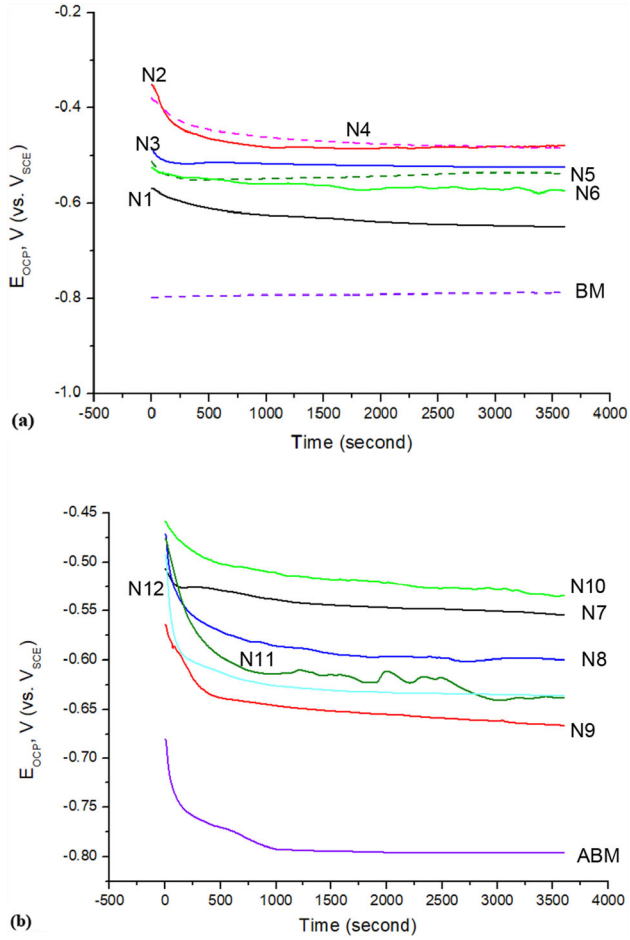

Fig. 18 OCP plots for (a) N1-N6 samples and BM, (b) N7-N12 samples and ABM

Figure 16(a), (b), (c), (d), (e) and (f) shows the worn surfaces of the gas-nitrided samples. In the wear test applied under 5 N load, microcracks were observed in N1 and N8 specimens (Fig. 16a, d). When the applied test load was 10 N, delamination was observed in N9 samples (Fig 16e), while only micro-cracks were determined in N4 (Fig. 16b). When the applied wear test was increased to 15 N, delamination was observed in all samples from N1 to N12. Delaminations were observed in N1-N6 samples in the wear tests applied under 15 N load. These results confirmed the wear volume results mentioned previously in Fig. 10 and 11. In addition, neither groove nor wear debris were detected in wear tracks of N1-N12. Wear debris is caused by fatigue fracture. The number of cycles of failure of contacts that cause wear debris depends on the fatigue limit of the sample. Therefore, an increase in the fatigue limit causes an increase in wear resistance (Ref 23). The absence of wear debris and grooves exhibits that the gas-nitriding process improves the wear resistance and fatigue limit of HMS.

Moreover, delaminations were observed in all gas-nitrided samples, however, they were seldom detected along the entire worn surface. Smooth layers were dominant on the worn surfaces of the gas-nitrided HMS specimens. The smooth layers consisted of an oxide layer which caused a wear-protective "glaze layer" (Ref 22). Figure 17 shows that the EDX

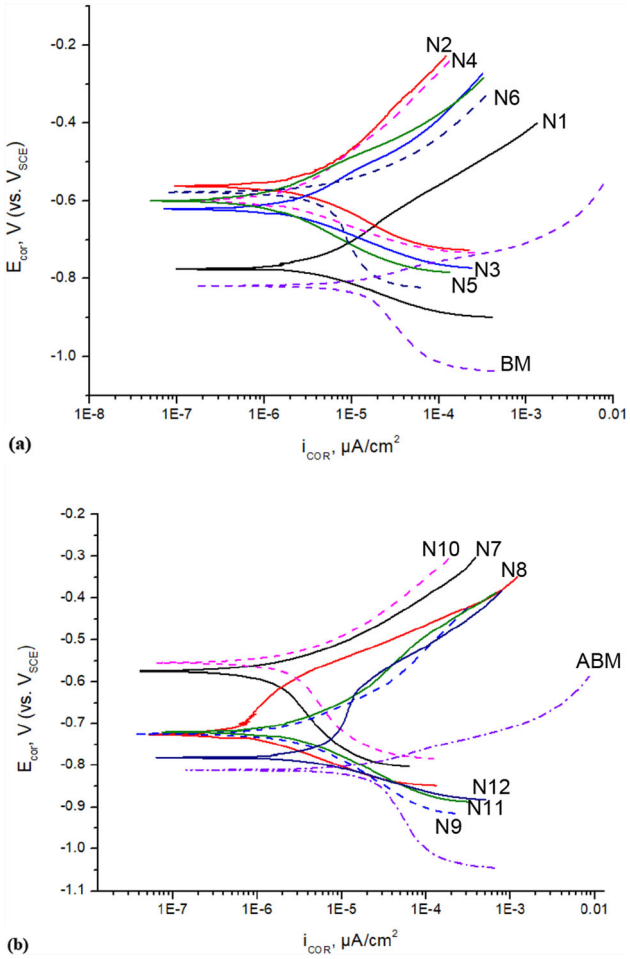

Fig. 19 Potentiodynamic polarization curves for (a) N1-N6 samples and BM, (b) N7-N12 samples and ABM

Table 4 Results of corrosion tests

Sample	E_{corr} (mV)	I_{corr} (μA10^{-2}/mm^2)	Corrosion rate (mpy)
ABM	− 808.5	8.8	3.57
BM	− 818.8	5.84	2.37
N1	− 776.9	2.96	1.2
N2	− 560.3	2.52	1.02
N3	− 619.2	1.63	0.66
N4	− 598.7	1.38	0.56
N5	− 594.9	0.94	0.38
N6	− 577.8	4.9	1.99
N7	− 574	2.08	0.84
N8	− 724.8	1.91	0.78
N9	− 724.4	4.25	1.73
N10	− 553.8	2.56	1.04
N11	− 719.7	2.37	0.96
N12	− 779.5	5	2.03

elemental analysis of the worn surface of the N12 sample confirms the smooth layer consists of the oxidation layer.

3.5 Corrosion Test

Figure 18 demonstrates that the curves of the open circuit potential (OCP) of the BM, N1-N6 samples (Fig. 18a) and ABM, N7-N12 samples (Fig. 18b) were obtained in 3.5% NaCl solution at room temperature. In Fig. 18a, the OCP values of gas-nitrided samples decreased for 500 seconds and then reached a steady potential. The OCP value of BM showed little if any increase (3 mV) for 1 hour. Figure 18b shows that the OCP values of gas-nitrided samples decreased for approximately 400 seconds, while that of the BM took almost 1000 seconds. The potentials of all samples then reached a steady state. Generally, while passive film formation on the surface increases the OCP value, uniform corrosion decreases the OCP value (Ref 39, 40).

The corrosion rate values of samples were evaluated using the potentiodynamic polarization tests and calculated with Eq 2. Figure 19 shows the polarization curves of all samples. Icorr and Ecorr were detected from Tafel plots in Fig. 19. In addition, Table 4 exhibits Icorr, Ecorr and corrosion rate values.

The Ecorr values of the samples ranged between − 818.8 and − 560.3 mV. The lowest and highest Ecorr values were observed in BM and N10, respectively. The results of the corrosion tests indicated that all gas-nitrided samples had nobler Ecorr values than untreated ABM and BM. Since the Ecorr of BM and ABM is more negative, the formation of metal ions is easier and hence they are more prone to corrosion.

Table 4 shows that the corrosion rate of BM was lower than that of ABM. The retained austenite has a different chemical reactivity from martensite, which can cause to galvanic attack at the interface between both of them (Ref 14). Hence, comparing with BM, retained austenite may have impaired corrosion resistance of ABM.

The corrosion rate of N1-N12 specimens is lower than that of BM and ABM. Since N5 had the lowest Icorr value and corrosion rate, the highest corrosion resistance was provided for HMS at 570 °C for 18 h. This parameter improved the corrosion resistance of the untreated base metal by 6 times. The high chemical stability of iron nitrides significantly improves the corrosion rate of HMS. In general, the samples with the expanded martensite layer exhibited better corrosion resistance than the others. The positive effect that reduces the corrosion rate can be the decrease in the pH of the media. As mentioned in the literature (Ref 14, 18, 41), when martensite rich in interstitial nitrogen atoms corrode, the free interstitial nitrogen atoms are released. When the N reacts with H^+, NH_4^+ occurs. It increases the local pH to facilitate the re-passivation.

In this study, no correlation was observed between corrosion rate and gas-nitriding parameters. Formation of complex phases on the surface, the crack formation, porosity and high surface roughness can cause non-correlation results (Ref 42).

Figure 20(a), (b), (c) and (d) shows the SEM images of corroded surfaces of samples N3, N9, BM and ABM,

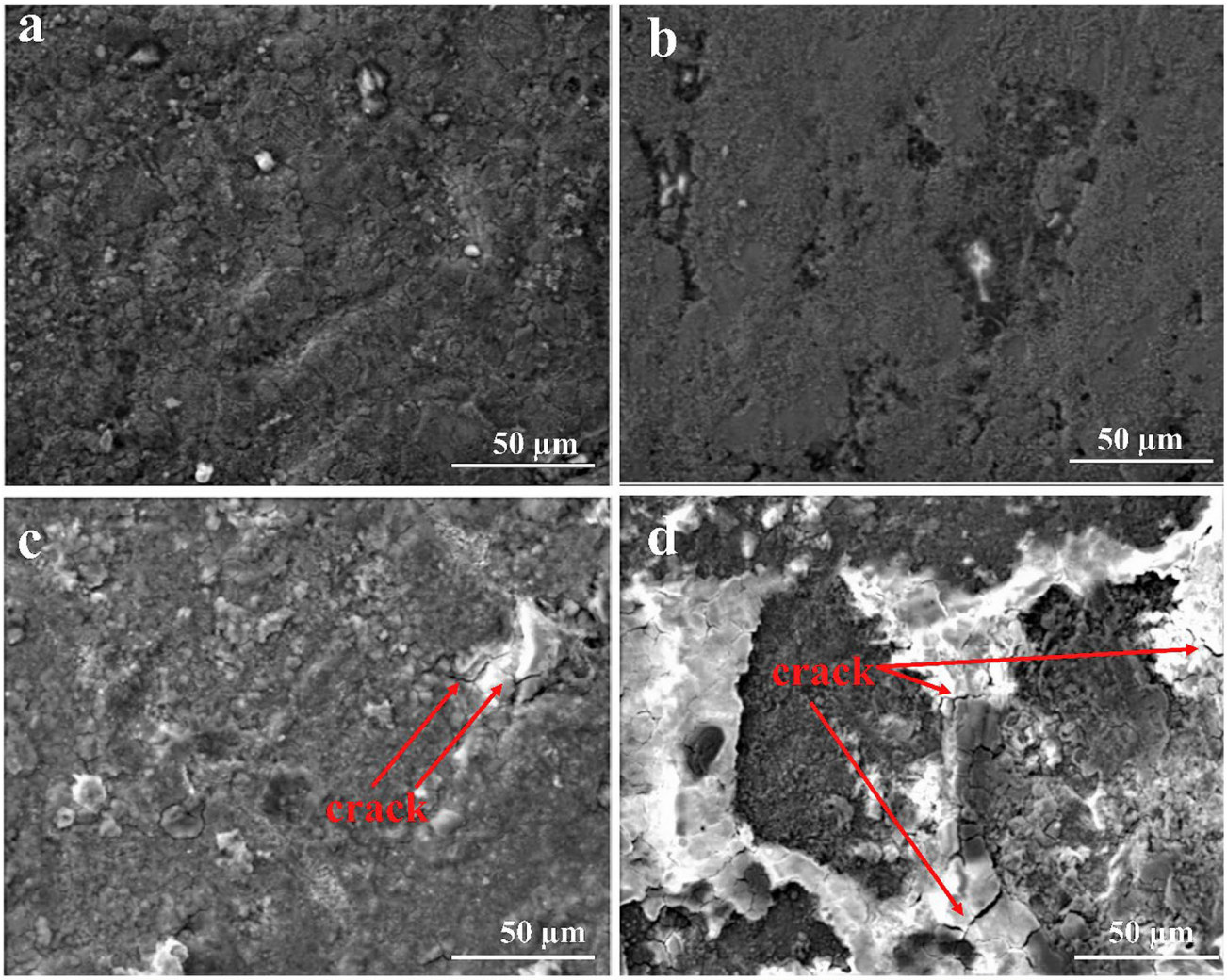

Fig. 20 SEM images of (a) N3, (b) N9, (c) BM and (d) ABM following the corrosion tests

Table 5 EDS elemental analyses of N3, N9, BM and ABM, wt.%

Sample	O	Fe	Mn	Si	N	Na	Cl
N3	47.5	41.8	6.6	0.8	2.9	0.1	0.3
N9	47.4	40.4	6.2	1.1	4.2	0.3	0.4
BM	42.2	47.3	7.1	2.1	…	0.2	1.1
ABM	47.2	43.2	6.1	1.7	…	0.8	1.0

respectively. It was determined that there was oxidation on the surfaces of all samples. While no crack or pit was observed in the N3 and N9 samples, cracks were detected in BM and ABM. The existence of cracks decreases the corrosion resistance of samples. This situation confirms the Tafel polarization result. Table 5 shows that the amount of chloride in ABM and BM is higher than in gas-nitrided samples. When the chloride ions penetrate into the cracks they can cause to increase the corrosion rate of samples.

4. Conclusions

In this study, tribological, adhesive and corrosive behavior of vacuum gas-nitrided HMS were investigated. The following conclusions can be drawn as follows:

BM contained α and ε martensite, while austenite was also observed in ABM. Although all gas-nitrided samples contain Fe_3N, Fe_4N, γ, α and ε martensite, the FeSi phase was only determined in N1-N6 samples. Expanded martensite and white layer (complex S phase) were observed in N1-N6 and N7-12, respectively. Thanks to the heat treatment before gas nitration, austenite was formed in the microstructure, which resulted in the formation of white layer instead of the expended martensite. The gas-nitriding significantly increased the surface hardness of HMS due to the iron nitride forming. According to the Daimler-Benz adhesion test, the adhesion quality of all gas-nitrided HMS is acceptable (HF1).

The roughness values of the ABM and BM were lower than gas-nitrided HMS. Generally, the COF values of gas-nitrided samples were lower than those of BM and ABM at all 3 loads. All of the gas-nitrided HMS showed higher wear resistance and lower wear rate for all wear test conditions than the ABM and BM. Micro-cracks, delamination, groove and wear debris were

detected on the surface of ABM and BM. However, wear debris and grooves were not observed in gas-nitrided samples. Since the expanded martensite surface (N1-N6) and white layer (N7-12) increase the hardness of the surface, the wear resistance and fatigue limit of HMS increases. It was observed that the wear volumes of the samples subjected to gas nitriding at 520 °C for 12 hours were less than the others. Although there was no exact correlation regarding the effect of increasing time and temperature on the wear volume, the wear volumes increased with the increase in temperature and time.

Tafel polorization test result shows that gas nitriding Tafel polorization test result shows that gas nitriding improves the lifespan of HMS significantly. In addition, no correlation was observed between the change in gas-nitriding parameters (temperature and time), and its effect on wear and corrosion resistance.

Acknowledgments

This study was supported by the Scientific Research Projects Coordination Unit of Karabük University (Project Number: FDK-2020-2114). The authors wish to thank Mehmet Kalkan.

Conflict of interest

The authors reported no potential conflict of interest.

References

1. Y.S. Ham, J.T. Kim, S.Y. Kwak, J.K. Choi, and W.Y. Yoon, Critical Cooling Rate on Carbide Precipitation During Quenching of Austenitic Manganese Steel, *China Foundry*, 2010, **7**(2), p 178–182.
2. S.H. Mousavi Anijdan, and M. Sabzi, The Effect of Heat Treatment Process Parameters on Mechanical Properties, Precipitation, Fatigue Life, and Fracture Mode of an Austenitic Mn Hadfield Steel, *J. Mater. Eng. Perform.*, 2018, **27**(10), p 5246–5253.
3. V. García-García, I. Mejía, H. Hernández-Belmontes, F. Reyes-Calderón, J.A. Benito, and J.M. Cabrera, Computational Simulation of Thermo-Mechanical Field and Fluid Flow and Their Effect on the Solidification Process in TWIP Steel Welds, *J. Manuf. Process.*, 2022, **84**, p 100–120.
4. K. Ding, Y. Wang, M. Lei, T. Wei, G. Wu, Y. Zhang, and Y. Gao, Numerical and Experimental Investigations on the Enhancement of the Tensile Shear Strength for Resistance Spot Welded TWIP Steel, *J. Manuf. Process.*, 2022, **76**, p 365–378.
5. N. Verma, A. Wasson, Z. Li, H. Sidhar, X. Yue, H. He, H.W. Jin, S. Ling, H.J. Jun, A. Ozekcin, *High Manganese Steel HMS Technology for Mooring Chains Application Offshore Technology Conference, Houston, Texas, May 2019, Paper Number: OTC-29246-MS*
6. X. Yue, A.J. Wasson, T.D. Anderson, N. Ma, D.P. Fairchild, and H. Jin, Welding Technology Development for an Erosion-Resistant Slurry Pipeline Steel: An Investigation into the Welding Technology Enabling the Deployment of an Erosion-Resistant Pipeline Steel in the Oil Sands Mining Industry to Achieve Significant Cost Savings, *Weld. J.*, 2018, **97**, p 229–242.
7. Y. Chen, X.M. Zhang, Z.H. Cai, Y.Q. Wang, and H. Ding, Effect of Microalloying with V and Ti on the Microstructure and Properties of Electron Beam Welded Thick High-Mn TWIP Steel Plates, *Mater. Sci. Eng. A*, 2021, **811**, 141062
8. M. Nagel, A. Tomitz, and J. Overrath, High-Manganese Steel for Ballistic Requirements, *Thyssen Krupp Techforum*, 2014, **1**, p 74–77.
9. J.N. Bestera and W.E. Stumpf, Material Characterization of a Novel New Armour Steel, *EPJ Web of Conferences*, 2012, **26**, p 01058.
10. R.A. Howell, J.S. Montgomery, and D.C. Van Aken, Advancements in Steel for Weight Reduction of P900 Armor Plate, *Iron Steel Technol.*, 2008, **6**, p 1–8.
11. S.J. Manganello and K.H. Abbott, Metallurgical Factors Affecting the Ballistic Behavior of Steel Targets, *J. Mater.*, 1972, **7**(2), p 231–239.
12. M. Übeyli, R.O. Yıldırım, and B. Ögel, On the Comparison of the Ballistic Performance of Steel and Laminated Composite Armors, *Mater. Des.*, 2007, **28**, p 1257–1262.
13. C. Yang and J. Liu, Intermittent Vacuum Gas Nitriding of TB8 Titanium Alloy, *Vacuum*, 2019, **163**, p 52–58.
14. G. Yan, S. Lu, M. Zhang, J. Wang, X. Yang, Z. Zhang, J. Gu, and C. Li, Wear and Corrosion Behavior of P20 Steel Surface Modified by Gas Nitriding with Laser Surface Engineering, *Appl. Surf. Sci.*, 2020, **530**, 147306
15. Z. Pokorný, D. Dobrocký, J. Kadlec, and Z. Studený, Influence of Alloying Elements on Gas Nitriding Process of High-Stressed Machine Parts of Weapons, *Kovove Mater.*, 2018, **56**, p 97–103.
16. P. Rajendran and A. Devaraju, Experimental Evaluation of Mechanical and Tribological Behaviors of Gas Nitride Treated AISI 316LN Austenitic Stainless Steel, *Mater. Today Proc.*, 2018, **5**, p 14333–14338.
17. J. Alphonsa, V.S. Raja, and S. Mukherjee, Study of Plasma Nitriding and Nitrocarburizing for Higher Corrosion Resistance and Hardness of 2205 Duplex Stainless Steel, *Corros. Sci.*, 2015, **100**, p 121–132.
18. H. Riazi, F. Ashrafizadeh, and A. Eslami, Effect of Plasma Nitriding Parameters on Corrosion Performance of 17–4 PH Stainless Steel, *Canad. Metall. Q.*, 2017, **56**(3), p 322–331.
19. X. Yuan, Y. Zhao, X. Li, and L. Chen, Effects of Gas Nitriding Temperature on the Surface Properties of a High Manganese TWIP Steel, *Metals*, 2017, **7**(3), p 102.
20. C.T. Sezgin and F. Hayat, The Effects of Boriding Process on Tribological Properties and Corrosive Behavior of a Novel High Manganese Steel, *J. Mater. Process. Technol.*, 2022, **300**, 117421
21. F. Hayat and C.T. Sezgin, Wear Behavior of Borided Cold-Rolled High Manganese Steel, *Coatings*, 2021, **11**(10), p 1207.
22. N. Vidakis, A. Antoniadis, and N. Bilalis, The VDI 3198 Indentation Test Evaluation of a Reliable Qualitative Control for Layered Compounds, *J. Mater. Process. Technol.*, 2003, **143–144**, p 481–485.
23. E.A. Dossantosdealmeida, C.E. Dacosta, and J.C.G. Milan, Study of the Nitrided Layer Obtained by Different Nitriding Methods, *Revista Matér.*, 2015, **20**(2), p 460–465.
24. Q.G. Zhu, H. Iwasaki, E.D. Williams, and R.L. Park, Formation of Iron Silicide Thin Films, *J. Appl. Phys.*, 1986, **60**, p 2629–2631.
25. C.L. Yeh and K.T. Chen, Synthesis of FeSi-Al_2O_3 Composites by Autowave Combustion with Metallothermic Reduction, *Metals*, 2021, **11**(2), p 258.
26. T. Masumura, T. Tsuchiyama, S. Takaki, T. Koyano, and K. Adachi, Difference Between Carbon and Nitrogen in Thermal Stability of Metastable 18%Cr–8%Ni Austenite, *Scr. Mater.*, 2018, **154**, p 8–11.
27. X.Y. Wang, Z.B. Chen, M.F. Yan, C.S. Zhang, H.T. Chen, and Y.D. Zhu, Preparation and Characterization of Ultra-Refined Expanded Martensite α′ N, *Surf. Coat. Technol.*, 2017, **326**, p 216–223.
28. Y.T. Xi, D.X. Liu, D. Han and Z.F. Han, Improvement of Mechanical Properties of Martensitic Stainless Steel by Plasma Nitriding at Low Temperature, *Acta Metall. Sin. (English Lett.)*, 2008, **21**(1), p 21–29.
29. S.K. Kim, J.S. Yoo, J.M. Priest, and M.P. Fewell, Characteristics of Martensitic Stainless Steel Nitrided in a Low-Pressure RF Plasma, *Surf. Coat. Technol.*, 2003, **163**, p 380–385.
30. A.P. Tschiptschin, A.S. Nishikawa, L.B. Varela, and C.E. Pinedo, Thermal Stability of Expanded Austenite Formed on a DC Plasma Nitrided 316L Austenitic Stainless Steel, *Thin Solid Films*, 2017, **644**, p 156–165.
31. T.L. Deepak, G.A. Mithra, K. Lokesh, B.S. Chandra, and R. Subbiah, Stability of Expanded Austenite by Gas Nitriding Process on Austenitic Stainless Steel Material Under Low Temperature Conditions, *Mater. Today Proc.*, 2020, **27**, p 1681–1684.
32. F.A. Fernandes, T.L. Christiansen, G. Winther, and M.A. Somers, Measurement and Tailoring of Residual Stress in Expanded Austenite on Austenitic Stainless Steel, *Mater. Sci. Eng. A*, 2017, **701**, p 167–173.
33. X. Yuan, Y. Zhao, X. Li, and L. Chen, Effects of Gas Nitriding Temperature on the Surface Properties of a High Manganese TWIP Steel, *Metals*, 2017, **7**(3), p 102.
34. L.H.P. Abreu, M.C.L. Pimentel, W.F.A. Borges, T.H.C. Costa, M. Naeem, J. Iqbal, and R.R.M. Sousa, Plasma Nitriding of AISI M2 Steel: Performance Evaluation in Forming Tools, *Surf. Eng.*, 2020, **36**(5), p 508–515.

35. F. Ashrafizadeh, Influence of Plasma and Gas Nitriding on Fatigue Resistance of Plain Carbon (Ck45) Steel, *Surf. Coat. Technol.*, 2003, **174**, p 1196–1200.
36. O. Unal, E. Maleki, and R. Varol, Effect of Severe Shot Peening and Ultra-Low Temperature Plasma Nitriding on Ti-6Al-4V Alloy, *Vacuum*, 2018, **150**, p 69–78.
37. K.H. Zum Gahr, *Microstructure and Wear of Materials*, Vol 10-Chapter 5 Elsevier, New York, 1987
38. M. Emami, H.M. Ghasemi and J. Rassizadehghani, High Temperature Tribological Behavior of 31CrMoV9 Gas Nitrided Steel, *Surf. Eng.*, 2010, **26**(3), p 168–172.
39. S. Jannat, H. Rashtchi, M. Atapour, M.A. Golozar, H. Elmkhah, and M. Zhiani, Preparation and Performance of Nanometric Ti/TiN Multi-Layer Physical Vapor Deposited Coating on 316L Stainless Steel as Bipolar Plate for Proton Exchange Membrane Fuel Cells, *J. Power. Sources*, 2019, **435**, p 1–10.
40. J. Xu, Z.Y. Li, S. Xu, P. Munroe, and Z.H. Xie, A nanocrystalline Zirconium Carbide Coating as a Functional Corrosion-Resistant Barrier for Polymer Electrolyte Membrane Fuel Cell Application, *J. Power. Sources*, 2015, **297**, p 359–369.
41. Y.T. Xi, D.X. Liu, and D. Han, Improvement of Corrosion and Wear Resistances of AISI 420 Martensitic Stainless Steel Using Plasma Nitriding at Low Temperature, *Surf. Coat. Technol.*, 2008, **202**(12), p 2577–2583.
42. M. Çetin, A. Günen, M. Kalkandelen, and M.S. Karakaş, Microstructural, Wear and Corrosion Characteristics of Boronized AISI 904L Superaustenitic Stainless Steel, *Vacuum*, 2021, **187**, 110145